Soft Tissue Deformation Tracking by Means of an Optimized Fiducial Marker Layout with Application to Cancer Tumors

Ye Han[1], Yoed Rabin[1], Levent Burak Kara[1*]

[1]Department of Mechanical Engineering
Carnegie Mellon University
Pittsburgh, PA 15213

*Corresponding author. lkara@cmu.edu

Preprint: Soft Tissue Deformation Tracking by Means of an Optimized Fiducial Marker Layout with Application to Cancer Tumors. Ye Han; Yoed Rabin; and Levent Burak Kara. International Journal of Computer Assisted Radiology and Surgery, 15(2): 225-237. 2020.

https://doi.org/10.1007/s11548-019-02075-0

Abstract

Objective: Interventional radiology methods have been adopted for intraoperative control of the surgical region of interest (ROI) in a wide range of minimally invasive procedures. One major obstacle that hinders the success of procedures using interventional radiology methods is the preoperative and intraoperative deformation of the ROI. While fiducial markers (FM) tracing has been shown to be promising in tracking such deformations, determining the optimal placement of the FM in the ROI remains a significant challenge. The current study proposes a computational framework to address this problem by preoperatively optimizing the layout of FM, thereby enabling an accurate tracking of the ROI deformations.

Methods: The proposed approach includes three main components: (i) creation of virtual deformation benchmarks, (ii) method of predicting intraoperative tissue deformation based on FM registration, and (iii) FM layout optimization. To account for the large variety of potential ROI deformations, virtual benchmarks are created by applying a multitude of random force fields on the tumor surface in physically based simulations. The ROI deformation prediction is carried out by solving the inverse problem of finding the smoothest force field that leads to the observed FM displacements. Based on this formulation, a simulated annealing approach is employed to optimize the FM layout that produces the best prediction accuracy.

Results: The proposed approach is capable of finding a FM layout that outperforms the rationally chosen layouts by 40% in terms of ROI prediction accuracy. For a maximum induced displacement of 20 mm on the tumor surface, the average maximum error between the benchmarks and our FM-optimized predictions is about 1.72 mm, which falls within the typical resolution of ultrasound imaging.

Conclusions: The proposed framework can optimize FM layout to effectively reduce the errors in the intraoperative deformation prediction process, thus bridging the gap between preoperative imaging and intraoperative tissue deformation.

Keywords

Tumor Deformation, Shape Reconstruction, Fiducial Markers, Layout Optimization, Stochastic Optimization, Laplace-Beltrami Operator

1. Introduction

Interventional radiology methods have been widely adopted by clinicians for monitoring surgical procedures. In a typical image-guided surgery, clinicians first perform an initial scan of the surgical region of interest (ROI). After medical images of the ROI are obtained, a preplan is created based on the reconstructed geometry of the ROI. During the procedure, the preplan is executed under the guidance of an intraoperative imaging modality such as ultrasound (US) or interventional MRI[1]. By using an intraoperative imaging modality, clinicians are able to observe the ROI while the patient is lying on the operating table. By registering the intraoperative observation with the reconstructed shape in clinicians' preplan, the ROI can be monitored, and thus reducing the risk of damaging important structures in the nearby anatomy.

One major obstacle in image-guided surgeries is the deformation of the tissue in the ROI. Since the biological tissues can be highly compliant, a slight change in a patient's posture may induce significant shape deformations of the tissue in the ROI, making it challenging for clinicians to match the intraoperative images with those obtained to construct the preplan. The time lag between preplanning and procedure may also permit tumor deformation due to the progression of the disease, an effect which is beyond the scope of the current study.

In an effort to overcome the challenge of geometric deformation, previous work has explored a variety of approaches to account and compensate for intraoperative tissue deformation. One extensively studied approach involves finding the complete deformation of ROI by combining the preoperative imaging data, the partial surface/selected point (sparse) data obtained during the procedure, and physically based simulations such as finite element method (FEM). In [2–5], researchers developed computational methods for predicting intraoperative liver deformations. There, the initial undeformed liver tissues were reconstructed from computed tomography (CT), and transformed into tetrahedral meshed to facilitate physically based simulations. During the tests/procedures, point matching algorithms were employed to establish the surface correspondence between the preoperative shape reconstructions and the intraoperative imaging data. Based on the computed surface correspondence information, the complete deformed shapes were constructed with insights on the choice of convergence scheme, deformation model, and boundary conditions. Recently, intraoperative measurement has been done to assess the fidelity of such deformation correction framework for liver surgery [6]. Along the same lines, other applications of this general approach have been demonstrated for predicting brain shift caused by tumor resection [7, 8] and intraoperative prostate registration [9]. Additionally, recent advances in computing hardware such as graphics processing unit (GPU) have enabled fast segmentation and 3D reconstruction of biological tissue directly from dense medical images [10].

A drawback of the above approaches is the difficulty in accurately establishing shape correspondence, as point matching algorithms are prone to producing mismatched regions especially in the absence of prominent anatomical features. In comparison, fiducial marker (FM) based registration offers a promising alternative. FMs can be bone screws, implanted spheres or adhesive skin markers [11]. Once the FMs are implanted/attached in and/or around the ROI, they

remain embedded in the tissue in the initial placement locations, thus allowing an accurate correspondence and tracking between their locations. Previous work has shown the feasibility of using FM tracking for predicting intraoperative deformation of soft tissue with high accuracy [12, 13].

There were previous studies on optimizing FM layout [11, 14] for rigid registration tasks, where the total registration errors were considered to be mainly resulted from fiducial localization/registration errors and the deformation behavior of soft tissue was not considered. Meanwhile, the FM optimization process was either to choose a subset of a limited number of pre-defined FM locations or to search close nearby regions, which did not allow a large enough searching space for the best possible FM layout.

In this study, a computational framework is proposed to optimize the placement (layout) of FMs such that the intraoperative prediction error of the entire tissue deformation can be minimized. Specifically, given the undeformed, 3D model of the tissue of interest, and the number of FMs that are to be used, our method identifies the best placement of the FMs such that the overall deformations of the tissue under a large variety of interstitial loads can be accurately predicted by only tracking the FMs during surgery. By allowing an accurate tracking of the tissue deformation, the ultimate goal of this work is to enable the image-based preoperative plans to be successfully administered intraoperatively where tissue deformation can otherwise present significant challenges.

The computation framework developed in this study is demonstrated on a minimally invasive procedure on a head-and-neck (H&N) tumor model, and the envisioned application follows three phases. In Phase I the tumor geometry is reconstructed using CT imaging at the diagnostics stage, and FM are strategically deployed using long hypodermic needles. Phase II is

performed offline, where preplanning of a minimally invasive procedure is considered, such as interstitial photodynamic therapy (IPDT) [15]. In Phase III, the preplan is targeted by using interventional ultrasound. Here, the location of the FM is first identified and, the deformed tumor shape is computed, a modified intraoperative plan is adopted, and the energy modality application is executed. The current study aims at bridging the gap between a well reconstructed tumor containing FM in Phase I and predication of the tumor shape at a later time in Phase III by computation tools, when only the FM are known to a high degree of certainty. Clinical challenges, such as the deployment of FM are not considered in this study. A previous study has demonstrated the feasibility of such an operation [12], while the current study aims at developing a strategy to best select the FM placement in Phase I. While IPDT and H&N cancer are presented here for illustration purposes, the computation framework proposed is quite general, and independent of the specific cancer or the applied minimally invasive energy modality.

2. Methods

The proposed framework consists of three main components: (i) creation of computational benchmarks as a way to simulate the variety of deformations that can be encountered, (ii) prediction of soft tissue deformation that takes place between the initial pre-surgical imagining and the actual surgery subject to changes in external forces, and (iii) optimization of FM layout to ensure tissue deformations can be predicted with the highest accuracy.

To illustrate our FM optimization framework, a H&N tumor model constructed from CT scanning is used in this study as shown in Fig.1(a). The original surface mesh model is noisy and anisotropically tessellated. In order to facilitate computation while maintaining the shape fidelity, Netgen [16] and Tetgen [17] are utilized for mesh simplification, surface smoothing and

volumetric mesh generation. The final tetrahedralized tumor model is shown in Fig.1(b). The mesh parameters are listed in Table 1.

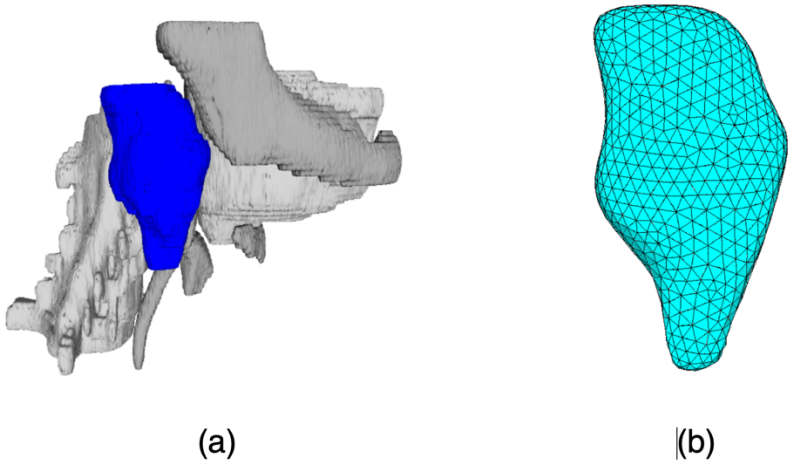

Figure 1: (a) Head-and-neck tumor model constructed from CT scanning. (b) The final tetrahedralized tumor model.

Table 1 Parameters of the mesh model in this study.

Parameter	Symbol	Model
Size	$dim_X \times dim_Y \times dim_Z$	19.9mm × 36.3mm × 67.9mm
Number of nodes	n	1158
Number of elements	n_e	4650
Number of surface nodes	n_s	760
Number of surface triangles	n_t	1516

2.1 Creation of Computational Benchmarks to Simulate Variety in Deformations

During image-guided surgeries, the true deformation of soft tissue matter in the ROI is challenging to predict accurately apriori. Depending on the nature of deformations (which is unknown a priori), the choice of the *optimal* FM layout for deformation prediction may also vary significantly. To overcome such difficulty, our strategy is to optimize the FM layout by simulating a large variety of deformations of the ROI (through different interstitial forces), and choosing the FM layout that overall minimizes the deformation prediction error over all such deformations. In

this section, the process of generating multiple ground truth deformations (benchmarks) is described in detail, where ground truth in this context refer to the virtually benchmarks generated from FEM simulations.

In this study, linear FEM with linear tetrahedral elements is used as the model to simulate tissue deformation. Without loss of generality, the current model can be easily extended to other FEM models with higher order elements and/or nonlinear FEM schemes. Through linear FEM [18], the relationship between the nodal displacements and forces is stated as Eq.(1),

$$Kx = f \tag{1}$$

where n is the total number or nodes, $K \in \mathbb{R}^{3n\times 3n}$ is the stiffness matrix, $x \in \mathbb{R}^{3n\times 1}$ is the displacement vector and $f \in \mathbb{R}^{3n\times 1}$ is the corresponding external load vector for all the nodes.

In order to create multiple benchmarks with realistic but varied deformations, a large variety of random smooth force fields are generated and applied to the tumor surface. The randomly created force fields ensure that benchmarks suitably span the space of possible deformations. Imposing smoothness on the simulated force fields is motivated by the observation that an anatomical ROI is commonly surrounded by soft tissue in its interstitial environment. If there is a change in the shape of ROI, the external loads that result in such changes are likely to be smoothly distributed over the ROI surface.

We employ the eigendecomposition of the discretized Laplace-Beltrami operator (LBO) defined over the surface of the tumor [19] as a way to parameterize the creation of random and smooth force fields on the tumor surface. For a given surface in the 3-dimensional (3D) space, the LBO can be constructed from the shape of the surface [20]. Suppose an arbitrary scalar function F is defined on the surface, mathematically any F can be reconstructed by taking the weighted sum of an infinite set of basis functions defined over this surface. In our approach, we use the

eigenfunctions of the LBO, which provide an appropriate basis for estimating F. These eigenfunctions are analogously similar to the vibratory mode functions (mode shapes) of the surface where displacements in response to forces can be represented as a weighted sum of the mode shapes.

In our work, we use this approach to generate force fields over the surface of the tumors. Based on the desire to simulate smooth force fields on the tumor surface, only a few low frequency components are needed to reconstruct F, which are the eigenfunctions with the smallest eigenvalues of the LBO. In the discretized case such as the triangulated surface we are working with, the LBO becomes the discretized LBO, which is constructed as an $n_s \times n_s$ matrix L using the cotangent scheme [21]. The corresponding eigenfunctions are obtained as the eigenvectors of the discretized LBO as shown in Fig.2(a). In order to illustrate these eigenvectors, the colormap in each subplot is adaptively adjusted based on the scale of the entries in each eigenvector. Each eigenvector is a vector with unit L_2 norm. The colormap maps the smallest value in the eigenvector to dark blue and the largest value to dark red in each subplot, with linear interpolation based on the color bar on the right side.

As can be seen in Fig.2(a), the first 15 eigenvectors already provide a set of low and high frequency components. In this paper, the $n_\phi = 15$ eigenvectors are employed as templates for constructing force fields. Depending on the actual scale of deformation and the size of the ROI, the number of extracted eigenvectors can be chosen empirically. After the eigenvectors are obtained, each benchmark force field is computed by following Eq.(2),

$$F_j = s_j \sum_{i=1}^{n_\phi} w_i \phi_i \; ; j = x, y, z \tag{2}$$

where F_j is the j^{th} component of a benchmark force field, s_j is the scaling factor, w_i is the weighting term sampled uniformly from $[-1, 1]$, and ϕ_i is the eigenvector with the i^{th} smallest

eigenvalue. The final load vector is obtained by concatenating the x, y and z components of each force field (which constructs a 3D force vector for each surface node) and multiplying each by per-node area to convert the force field into nodal forces on the surface. The per-node area is computed as Eq.(3),

$$A_i = \frac{1}{3}\sum_{j=1}^{n_j} a_{ij} \tag{3}$$

where A_i is the per-node area of node i, n_j is the number of triangle adjacent to node i and a_{ij} is area of the j^{th} adjacent triangle.

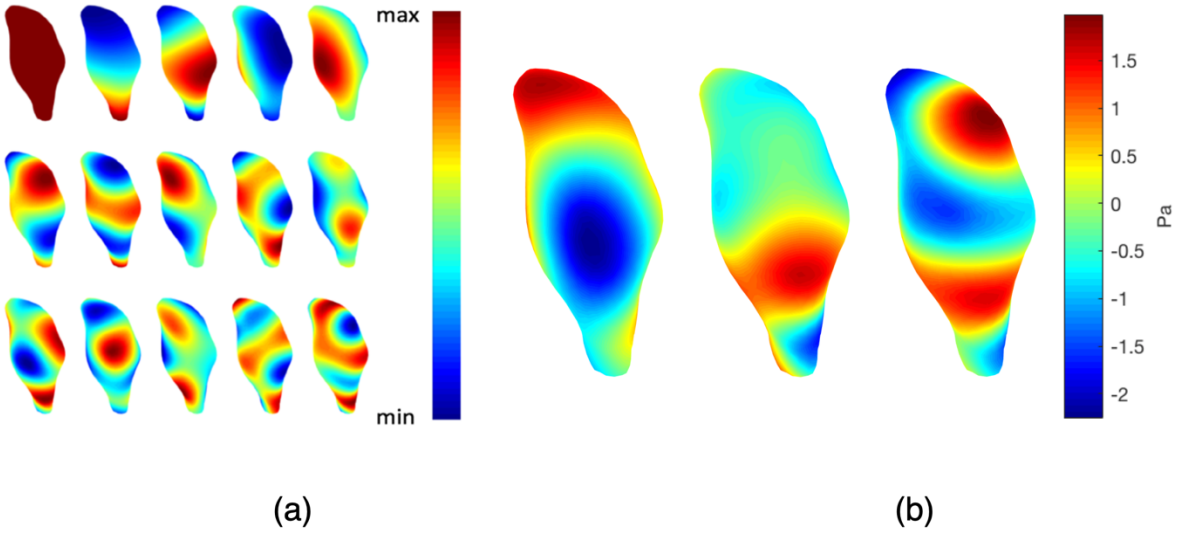

Figure 2: (a) First 15 eigenvectors of discretized LBO with the smallest eigenvalues. The color of each surface is adaptively self-mapped using the color bar on right side. (b) x, y and z components of a benchmark force field obtained from the weighted sum of the eigenvectors.

To produce shape deformations that are realistic relative to the size of the tumor, the maximum absolute surface displacements of the benchmarks need to be limited. For each benchmark model, we ensure this by first computing the original displacements in response to the created force fields and then scaling up (or down) the applied forces linearly to achieve the target maximum displacements. In our approach, since the displacements are linear in the weights of the

eigenvectors used to construct the force fields, this scaling is easily achieved through an amplification or attenuation of the eigenvector weights by a single scalar factor.

Finally, we compute deformed tumor shapes (benchmarks) by following the scheme described above. These benchmarks will be regarded as the ground truth to evaluate our shape prediction method in later sections.

2.2 Deformation Prediction

During the shape prediction process, we employ the approach described in [12] which demonstrates the ability to predict the deformed tumor shapes with high accuracy based solely on the observed displacements of the FMs. The deformation prediction is achieved by computationally identifying the smoothest force field on the tumor surface, such that the FMs in the deformed shape match their observed locations in the benchmarks. To achieve high prediction accuracy, larger number of FMs n_D is preferred. Meanwhile, with the consideration of the tumor size and the practical preference for fewer FMs, the number of FM is chosen to be $n_D = 5$ in this study. The mathematical formulation is briefly described as following:

By switching the lines of K and f, Eq.(1) can be rewritten in the form of Eq.(4),

$$\begin{bmatrix} K_u \\ K_l \end{bmatrix} x = \begin{bmatrix} f_u \\ f_l \end{bmatrix} \tag{4}$$

where the lines of K_u and f_u correspond to the surface nodes, and lines of K_l and f_l corresponds to the nodes inside the tumor. The prediction of deformed shape is obtained by solving the quadratic programming optimization problem in Eq.(5),

$$\underset{x}{\operatorname{argmin}}\, x^T K_s x \text{ subject to } \begin{cases} Dx = d \\ K_l x = 0 \end{cases} \tag{5}$$

where $K_s = (L_3 M K_u)^T (L_3 M K_u)$, $L_3 \in \mathbb{R}^{3n_s \times 3n_s}$ is the 3 dimensional discretized LBO obtained by assembling L in the way x is indexed [11], M is the diagonal inverse mass matrix that converts the nodal forces to a pressure field on the tumor surface in FEM whose i^{th} diagonal element equals

to $\frac{1}{A_i}$ in Eq.(3), $D \in \mathbb{R}^{3n_D \times 3n}$ is a binary indicator matrix which specifies the selection of FMs, and the $d \in \mathbb{R}^{3n_D \times 1}$ is the observed displacements of the corresponding FMs in the benchmarks. Setting Dx to d ensures that the FMs move to their observed locations in the benchmarks. By the assumption that no external forces are applied to the internal nodes, the load vector of the internal nodes f_l is set to 0. With the quadratic formulation described in Eq.(5), we aim to obtain the smoothest force distribution on the tumor surface such that the above constraints are satisfied. Since the final prediction only depends on the choice of the FM layout, the final output of the prediction process can be written in the form of Eq.(6),

$$x_{pred} = R(D) \tag{6}$$

where $x_{pred} \in \mathbb{R}^{3n \times n_b}$ is the nodal displacements of the predicted tumor shapes, and R is the prediction function that maps D to x_{pred}.

2.3 Optimization of FM Layout

We use simulated annealing (SA) [22] to optimize the FM layout for shape prediction. During the initial shape prediction, n_d FMs are randomly selected from the nodes of the mesh model. The initial prediction error Err_{old} is then computed as the Frobenius norm of the difference between the surface nodal displacement matrices of the benchmarks x_{bench} and the initial predictions x_{pred} (Eq.(7)).

$$Err_{old} = \left|\left|x_{pred} - x_{bench}\right|\right|_{fro}^{2} \tag{7}$$

The Frobenius norm allows a suitable balance between the *mean* offset (1-norm) and *maximum* offset (infinite-norm), which we want to minimize simultaneously. While our study uses the Frobenius norm, any norm between 1-norm and infinite-norm, or a weighted sum of multiple norms, could be employed as the error function to be minimized without loss of generality.

After the initial prediction, the SA scheme iteratively improves the prediction accuracy by testing neighborhood FM layouts. During each iteration, a new FM layout is selected randomly from the mesh vertices where each new FM is within δ distance of the current FM set. The new FM layout is accepted if its prediction error Err_{new} is less than Err_{old}. Otherwise, the new FM layout is accepted with a probability of $p = \exp\left(\frac{Err_{old} - Err_{new}}{T}\right)$ where T is the temperature at current iteration. A description of the SA-based layout optimization is shown in Fig.3. The SA process is terminated after reaching a pre-defined maximum number of iterations n_{max}. The parameters of the SA process used in the current study are listed in Table 2. The initial temperature T_i is selected to be high enough such that p is very large in the first few iterations. This ensures new FM layouts in the early iterations can be accepted with high probability even if they are not good choices, so as to prevent SA from getting stuck in local minima. The initial neighborhood size is also set to be large such that the FMs can move broadly over the tumor domain. This is to help the final optimized FM layout to be less sensitive to the initial FM layout. As the iterative optimization process proceeds, the temperature T and neighborhood size δ get updated by multiplying c_t and c_δ respectively in each iteration. The updating scheme decrease T and δ so that the preference of accepting new FM layout gradually shifts to nearer neighboring layout with better prediction accuracy.

Table 2: Selected parameters for SA process.

Parameter	Symbol	Value
Initial temperature	T_i	$1 \times 10^0 K$
Final temperature	T_f	$5 \times 10^{-5} K$
Initial neighborhood size	δ_i	$3 \times 10^{-2} m$
Final neighborhood size	δ_f	$4 \times 10^{-3} m$
max number of iterations	n_{max}	200

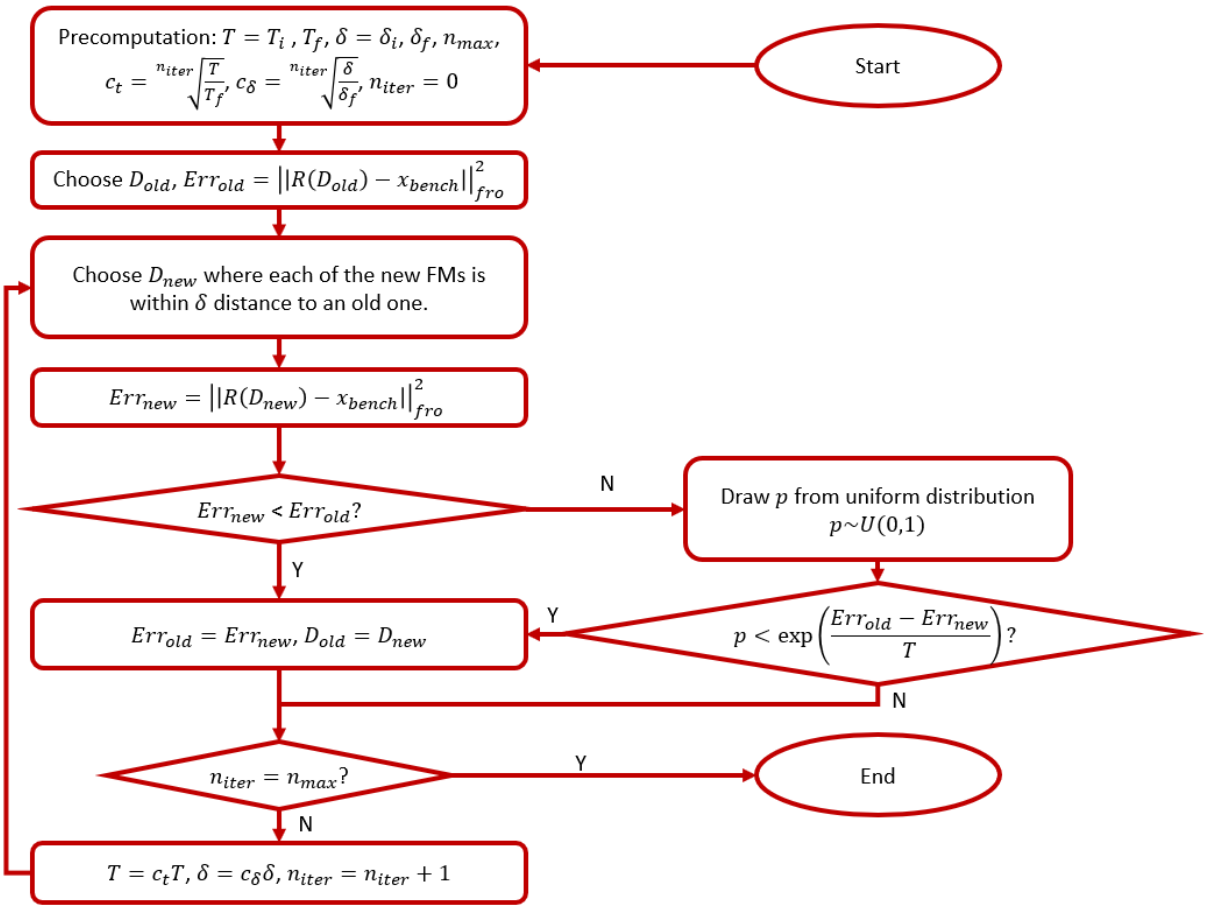

Figure 3: Flow chart of the FM optimization process.

2.4 Performance Evaluation

The evaluation procedure of our FM optimization framework is described in below:

1. Create a training set of $n_B = 1000$ deformation benchmarks using the scheme described in Section 2.1. The maximum absolute surface displacements are limited with a uniform distribution between 5 mm and 25 mm, which reflects a reasonable range of deformation based on the tumor size.
2. Optimize the FM layout with the n_B benchmarks in the training set. The optimization process is run 20 times with randomly selected initial FM layouts, for the purpose of obtaining converging statistics.

3. The optimized layout is tested on two unseen benchmark sets, with the maximum absolute surface displacements of 10 mm and 20 mm respectively. Each benchmark set contains $n_T = 1000$ benchmarks for evaluating FM layout optimization performance. Error functions of rationally selected FM layouts are also computed and compared with the optimized FM layout.
4. Use the optimized FM layout as the datum, and place each FM to nearby region randomly with distances between 0 mm and 5 mm. Evaluate how optimization objective changes after such fiducial localization error is introduced.

3. Results and Discussion

In this study, a training set of $n_B = 1000$ deformation benchmarks are created by following the scheme described in Section 2.1 for optimizing FM layout. Given the size of the tumor in Table 1, we limit the maximum absolute surface displacements to be between 5 mm and 25 mm. The visual comparisons between the initial undeformed (blue) and the deformed (green) benchmarks are shown in Fig.4. As can be seen in Fig.4, the proposed benchmark creation scheme is capable of producing a rich set of variations in the deformed shapes.

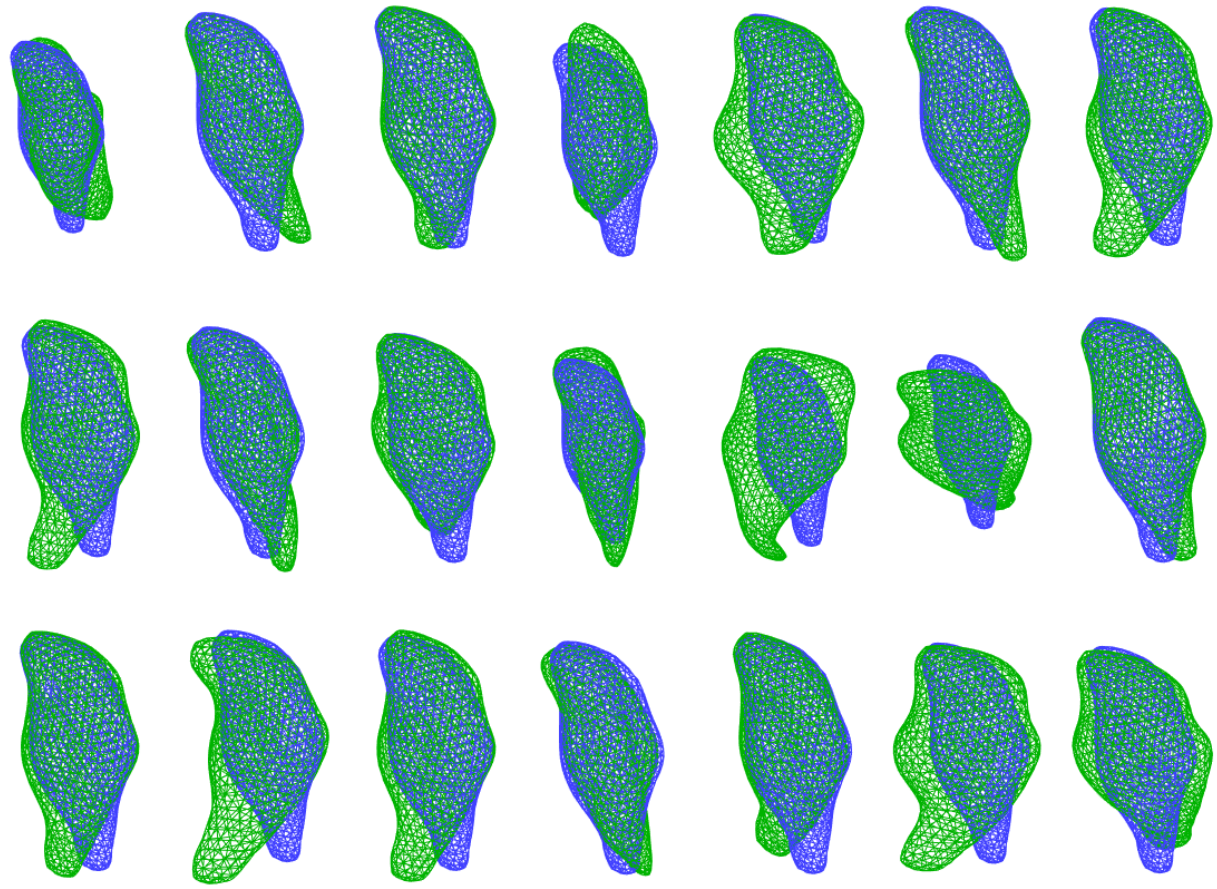

Figure 4: Visual comparisons between the initial undeformed shapes (blue) and the deformation benchmarks (green) where the maximum displacements on tumor surface ranges between 5 mm and 25 mm.

To evaluate our SA algorithm, the optimization process is run 20 times with randomly selected initial FM layouts. Fig.5 shows the prediction errors in mean Frobenius norm (objective function value) between initial FM layouts, optimized FM layouts and optimized layouts with fiducial localization error (FLE) across 20 runs of the FM layout optimization process. With the selected initial SA temperature and neighborhood size, the results generally converge to the same prediction accuracy for each case, without a noticeable dependency on the initial FM layout. Fig.6 shows the initial FM layout, trajectories of the FMs over the iterations, and the final FM layout for one run. From Fig.6, our SA algorithm can move the FMs far away from their initial locations as a way to explore the large space of possible FM layouts.

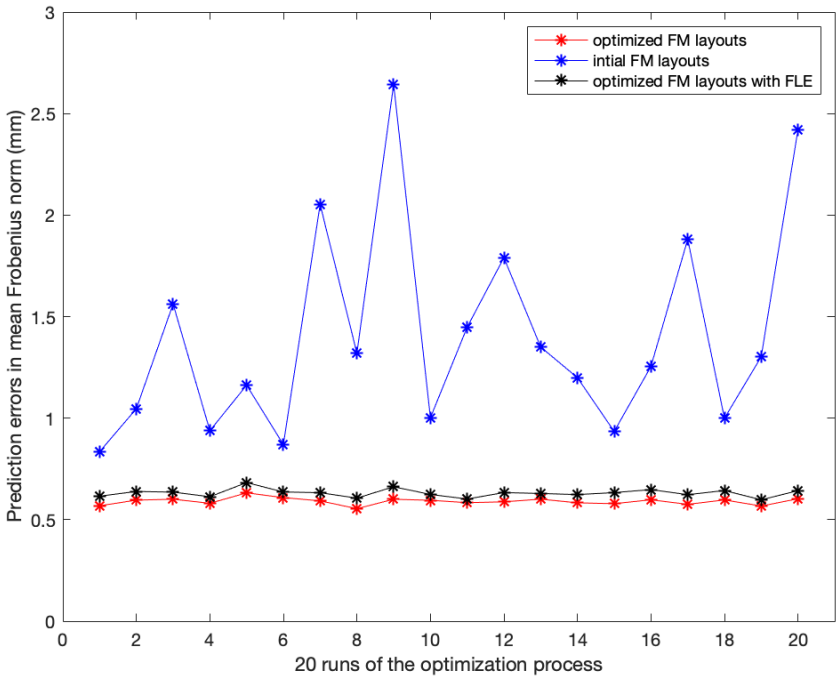

Figure 5: Differences in Frobenius norm (error function) between initial FM layouts, optimized FM layouts, and optimized FM layouts with FLE across 20 runs of the FM layout optimization process.

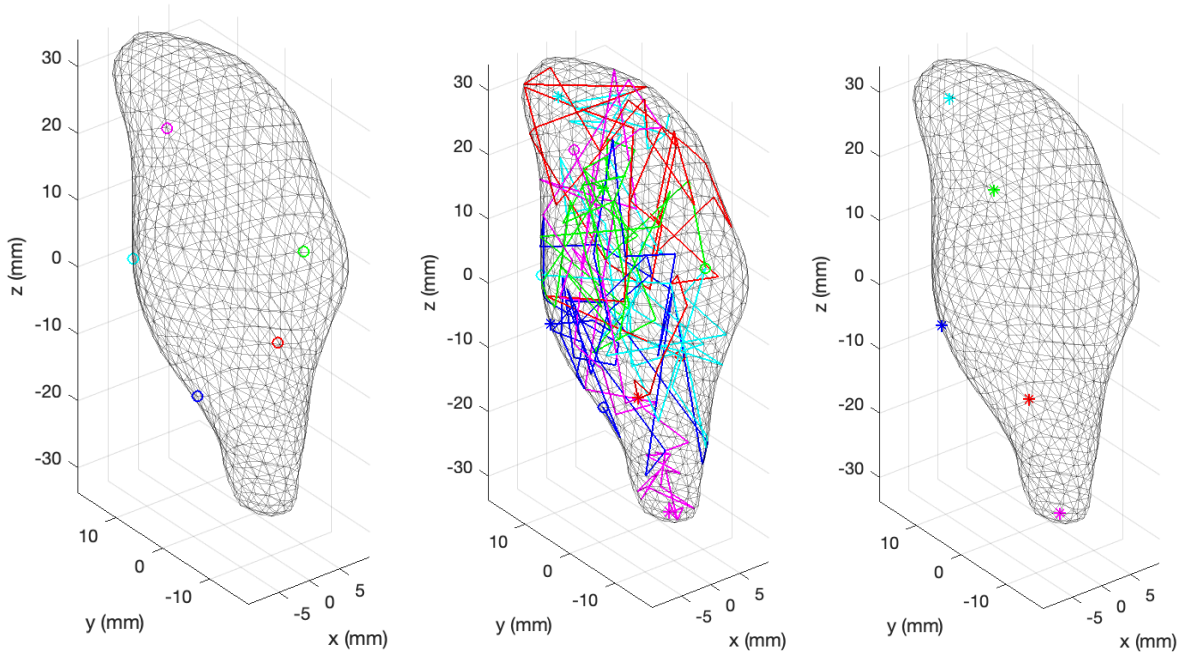

Figure 6: The initial FM layout (a), trajectories of the FMs over the SA iterations (b) and the final, optimized FM layout (c) for an optimization run.

The prediction errors over the iterations in one run is shown in Fig.7. Four error functions between the benchmark surfaces and predictions are plotted including the Frobenius norm (as described in Section 2.3), the 4-norm, mean offset (1-norm) and maximum offset (infinity-norm). In general, the four error functions follow a similar downward trend as the FM layout is iteratively optimized. This observation implies that both the average (mean) error as well as the maximum error in the nodal position predictions desirably decrease as the FM layout is improved. As seen both in Fig.7, the prediction errors change significantly in the first few iterations. This is due to the high initial temperature and the large initial neighborhood size in SA as described in Section 2.3. As the temperature decreases over the iterations, the new FM layouts that produce a larger error compared to the previous iteration are accepted with a monotonically decreasing probability. Towards the end of the SA iterations, our algorithm only accepts FM layouts with smaller prediction error between consecutive iterations. The final result converges to an FM layout with the smallest prediction error in its neighborhood. Over all the iterations in both runs, the mean offset between the benchmarks and predictions is always below 1 mm which is the typical resolution of the US imaging. This means that our deformation prediction approach is able to predict the deformed tumor with high fidelity. In terms of the maximum offset among all benchmarks, the error drops from 31 mm to 9 mm. Note that these maximum offsets are for one benchmark in training set. The average maximum offset for all 1000 benchmarks is 1.3 mm, with distribution shown in Fig.8. Also, the error values are calculated by aggregating the error between each node on the surface of the tumor in the ground truth deformation and the same point's location in the predicted deformation model. This is in contrast to a less stringent measure of calculating, for each ground truth surface node, the shortest distance to the predicted deformation model. As

such, our calculated maximum offsets are conservative in that they overestimate the actual mismatch between the ground truth and predicted model.

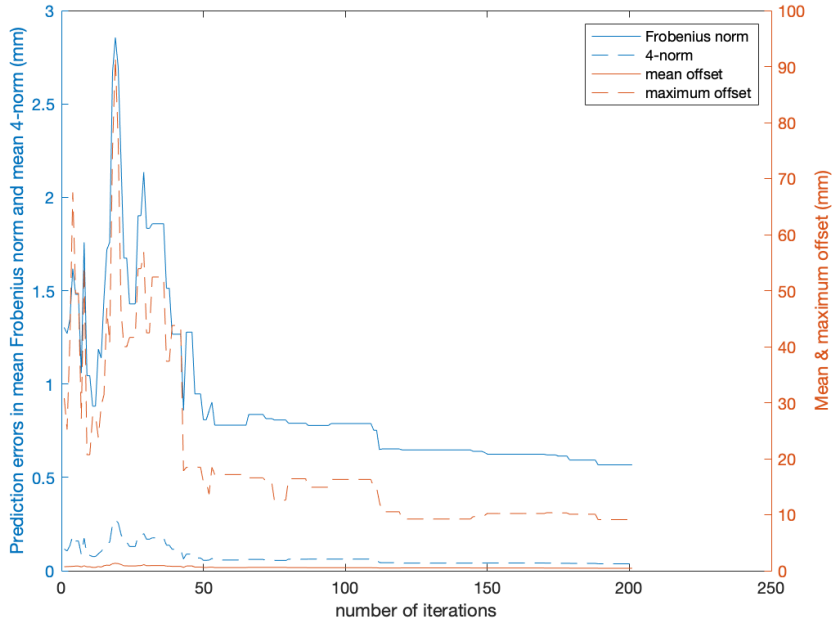

Figure 7: Changes in prediction errors over the SA iterations in one run of the training benchmark set.

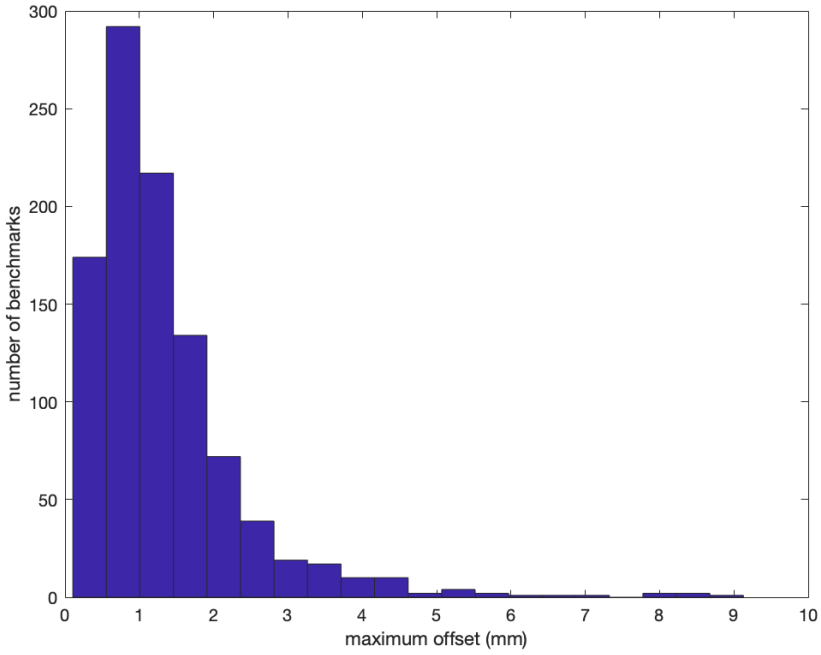

Figure 8: Distribution of maximum offsets for the 1000 benchamarks in the training set using the optimized FM layout.

In order to comprehensively evaluate the performance of our SA algorithm, the optimized FM layout is compared with rationally selected FM layouts such as FM placements at high curvature points, metric k-centers [23], and axis-aligned extrema (Fig.9). The tests are performed on two sets of unseen benchmarks, which are created with the maximum absolute surface displacements of 10 mm and 20 mm respectively. Each test set contains $n_T = 1000$ benchmarks. The evaluation is based on the average mean and average maximum surface offsets. Since the maximum offsets show high variations across benchmarks, to provide better understanding of the test results, a Gamma distribution $f(x) = \frac{x^{\kappa-1}e^{-\frac{x}{\theta}}}{\theta^{\kappa}\Gamma(\kappa)}$ is fitted to each maximum-offset entry in Table 3 based on the statistics in Fig.8. The fitted parameters of the Gamma distributions are provided as the shape parameter κ and scale parameter θ. As shown in Table 3, our SA algorithm is able to find an FM layout that outperforms those rational selections. The average maximum surface offset between the benchmarks and our FM-optimized prediction is 0.89 mm and 1.72 mm on average for the 10 mm and 20 mm benchmark sets respectively. The results indicate an approximately 40% decrease in the deformation prediction error when compared with the predicted shapes using rationally selected FM layouts.

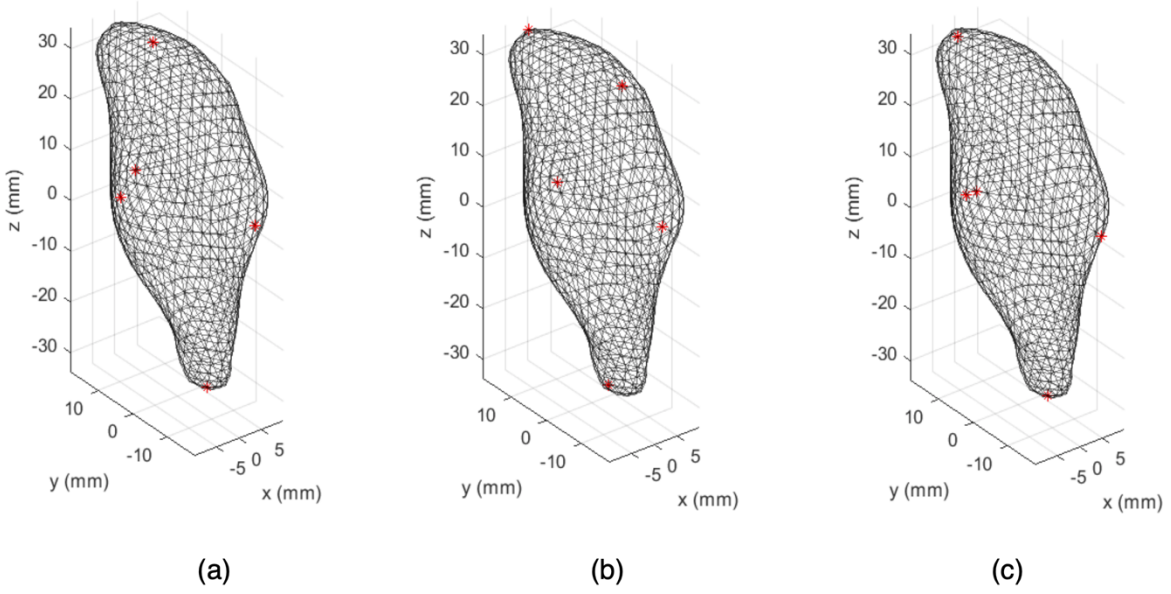

Figure 9: Rational selections of FM layout: (a) axis-aligned extrema (b) high curvature points and (c) metric k-centers.

Table 3: Prediction accuracies from different choices of FM layout with fitted Gamma distribution parameters.

Selection for FMs	10 mm maximum displacement		20 mm maximum displacement	
	Average mean offset (mm)	Average maximum offset (mm) (κ, θ)	Average mean offset (mm)	Average maximum offset (mm) (κ, θ)
Axis aligned extrema	0.43	1.35 (3.12, 0.43)	0.82	2.64 (3.14, 0.84)
High curvature points	0.44	1.50 (2.84, 0.60)	0.85	2.95 (2.59, 1.14)
Metric k-centers	0.42	1.32 (3.05, 0.43)	0.80	2.58 (3.17, 0.81)
Random layout	0.48	2.94 (2.25, 1.31)	0.95	5.90 (2.15, 2.74)
Optimized layout (proposed)	0.30	0.89 (3.49, 0.26)	0.57	1.72 (3.57, 0.48)

The benchmark with the maximum surface offsets in the 20 mm test set is shown in Fig.10. The points with the largest prediction error tend to be located near the tip of the tumor. This observation suggests a practical strategy that, if decided manually without computational support, adding FMs around the tips of elongated regions may help increase tracking fidelity in terms of

maximum offset, as the FMs near those regions would lead to more precise information gathering near such regions.

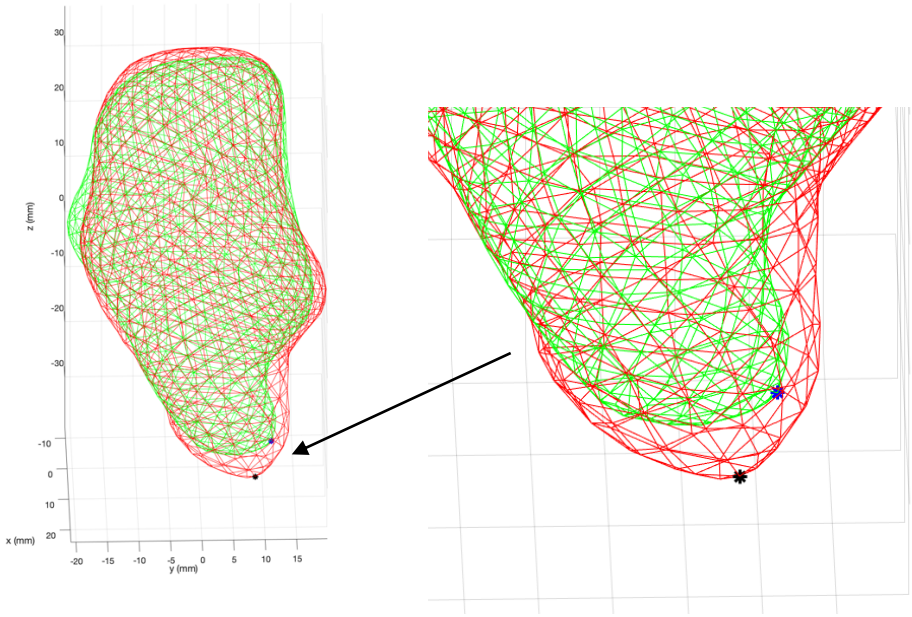

Figure 10: prediction result with the maximum offset in the 20 mm set with benchmark deformations (green), predictions (red), and maximum offset points on benchmark (blue) and predictions(black).

Another practical factor related to this work is the FLE. In an amorphous shape like the tumor, the FMs may not be localized accurately to the targeting location. A study on FLE is performed. An FLE within the range of 0 mm to 5 mm is added each of the optimized FMs. Fig.11 shows how the prediction error changes as the FLE increases. From Fig.11, it can be seen that the prediction error increases along with the increase in FLE of each FM.

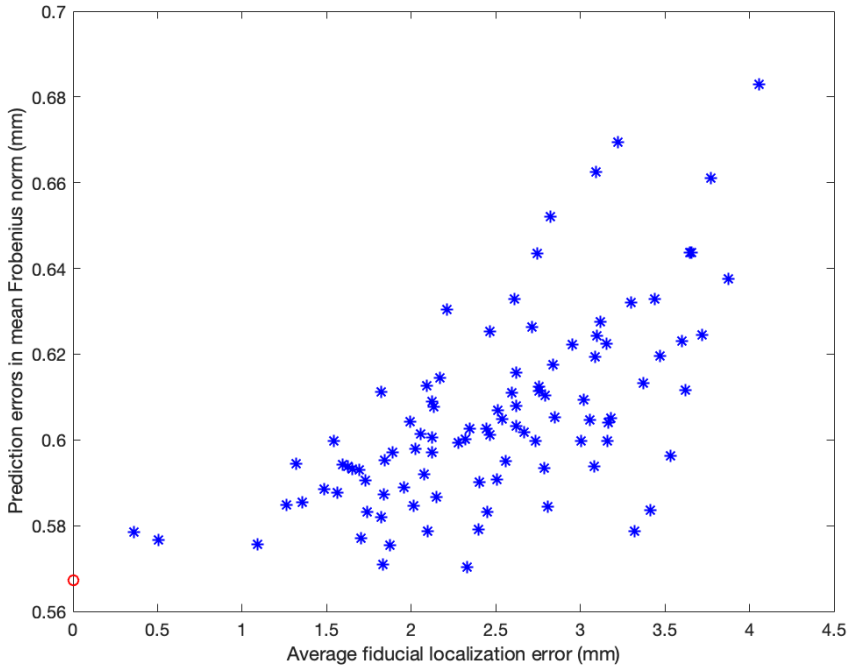

Figure 11: Changes in prediction error when FLE is added to the optimzed FM layout.

Overall, the presented work has demonstrated our optimization framework's ability to improve the prediction accuracy in FM-based approach for tracking soft tissue deformations. Such improvement can provide clinicians with better visualization of the deformed shape of ROI during the procedure.

4. Summary and Conclusions

As a proof of concept, a computational framework has been developed to optimize FM layout for tracking tissue deformation. The framework includes three main steps: (i) creation of benchmarks, (ii) deformation prediction and (iii) optimization of FM layout for better prediction accuracy. During the creation of benchmarks, the eigendecomposition of the discretized Laplace-Beltrami Operator is employed for creating multiple benchmark deformations, which are used as ground truths to emulate the large space of potential deformations. In the deformation prediction, an approach based on FEM and quadratic programming is utilized to predict the deformed shape

from the observed displacements of the FMs. Finally, simulated annealing is employed for optimizing the FM layout for minimizing the prediction error. From the FM layout optimization results, the prediction accuracy using the optimized FM layout is superior to those using rationally selected FM layouts. In terms of the maximum surface offset, the prediction errors on both 10 mm and 20 mm sets are reduced by approximately 40% over the rationally chosen layouts, while maintaining the sub-resolution accuracy in average surface offset. Overall, the applications of FMs and the presented FM optimization framework can bridge the gap between preplanning and intraoperative US imaging for the purpose of accurate tumor destruction.

5. Acknowledgement

Authors would like to thank Prof. Gal Shafirstein and Roswell Park Comprehensive Cancer Center for providing anatomical geometries from CT scanning.

6. Compliance with Ethical Standards

Conflict of Interest: The authors declare that they have no conflict of interest.

Ethical approval: All procedures performed in studies involving human participants were in accordance with the ethical standards of the institutional and/or national research committee and with the 1964 Helsinki declaration and its later amendments or comparable ethical standards.

Informed consent was obtained from all individual participants included in the study.

7. Reference

1. Barkhausen J, Kahn T, Krombach GA, Jörg Barkhausen, Thomas Kahn, Gabriele A. Krombach, Kuhl CK, Lotz J, Maintz D, Ricke J, Schönberg SO, Vogl TJ, Wacker FK, German Association of Chairmen in Academic Radiology (KLR) (2017) White Paper: Interventional MRI: Current Status and Potential for Development Considering Economic Perspectives, Part 1: General Application. ROFO Fortschr Geb Rontgenstr Nuklearmed 189:611–623. https://doi.org/10.1055/s-0043-110011

2. Cash DM, Miga MI, Sinha TK, Galloway RL, Chapman WC (2005) Compensating for intraoperative soft-tissue deformations using incomplete surface data and finite elements. IEEE Trans Med Imaging 24:1479–1491. https://doi.org/10.1109/TMI.2005.855434

3. Rucker DC, Wu Y, Clements LW, Ondrake JE, Pheiffer TS, Simpson AL, Jarnagin WR, Miga MI (2014) A Mechanics-Based Nonrigid Registration Method for Liver Surgery Using Sparse Intraoperative Data. IEEE Trans Med Imaging 33:147–158. https://doi.org/10.1109/TMI.2013.2283016

4. Hsu WJ, Ho MC, Lian FL, Yen JY, Lin WL, Chen YY (2015) Computation of liver deformations for minimally invasive surgery. In: 2015 International Automatic Control Conference (CACS). pp 7–12

5. Heiselman JS, Clements LW, Collins JA, Simpson AL, Geevarghese SK, Kingham TP, Jarnagin WR, Miga MI (2017) Characterization and correction of intraoperative soft tissue deformation in image-guided laparoscopic liver surgery. J Med Imaging 5:021203. https://doi.org/10.1117/1.JMI.5.2.021203

6. Clements LW, Collins JA, Weis JA, Simpson AL, Kingham TP, Jarnagin WR, Miga MI (2017) Deformation correction for image guided liver surgery: An intraoperative fidelity assessment. Surgery 162:537–547. https://doi.org/10.1016/j.surg.2017.04.020

7. Lunn KE, Paulsen KD, Roberts DW, Kennedy FE, Hartov A, Platenikb LA (2003) Nonrigid brain registration: synthesizing full volume deformation fields from model basis solutions constrained by partial volume intraoperative data. Comput Vis Image Underst 89:299–317. https://doi.org/10.1016/S1077-3142(03)00005-5

8. Sun K, Pheiffer TS, Simpson AL, Weis JA, Thompson RC, Miga MI (2014) Near Real-Time Computer Assisted Surgery for Brain Shift Correction Using Biomechanical Models. IEEE J Transl Eng Health Med 2:1–13. https://doi.org/10.1109/JTEHM.2014.2327628

9. Khallaghi S, Sánchez CA, Rasoulian A, Sun Y, Imani F, Khojaste A, Goksel O, Romagnoli C, Abdi H, Chang S, Mousavi P, Fenster A, Ward A, Fels S, Abolmaesumi P (2015) Biomechanically Constrained Surface Registration: Application to MR-TRUS Fusion for Prostate Interventions. IEEE Trans Med Imaging 34:2404–2414. https://doi.org/10.1109/TMI.2015.2440253

10. Smistad E, Falch TL, Bozorgi M, Elster AC, Lindseth F (2015) Medical image segmentation on GPUs – A comprehensive review. Med Image Anal 20:1–18. https://doi.org/10.1016/j.media.2014.10.012

11. Shamir RR, Joskowicz L, Shoshan Y (2012) Fiducial Optimization for Minimal Target Registration Error in Image-Guided Neurosurgery. IEEE Trans Med Imaging 31:725–737. https://doi.org/10.1109/TMI.2011.2175939

12. Han Y, Oakley E, Shafirstein G, Rabin Y, Kara LB (2018) Reconstruction of a Deformed Tumor Based on Fiducial Marker Registration: A Computational Feasibility Study. Technol Cancer Res Treat 17:1533034618766792. https://doi.org/10.1177/1533034618766792

13. Nimsky C, Ganslandt O, Hastreiter P, Fahlbusch R (2001) Intraoperative compensation for brain shift. Surg Neurol 56:357–364. https://doi.org/10.1016/S0090-3019(01)00628-0

14. Franaszek M, Cheok GS (2017) Selection of fiducial locations and performance metrics for point-based rigid-body registration. Precis Eng 47:362–374. https://doi.org/10.1016/j.precisioneng.2016.09.010

15. Brodin NP, Guha C, Tomé WA (2015) Photodynamic Therapy and Its Role in Combined Modality Anticancer Treatment. Technol Cancer Res Treat 14:355–368. https://doi.org/10.1177/1533034614556192

16. Schöberl J (1997) NETGEN An advancing front 2D/3D-mesh generator based on abstract rules. Comput Vis Sci 1:41–52. https://doi.org/10.1007/s007910050004

17. Si H (2015) TetGen, a Delaunay-Based Quality Tetrahedral Mesh Generator. ACM Trans Math Softw 41:11:1–11:36. https://doi.org/10.1145/2629697

18. Bathe KJ (1996) Finite Element Procedures. Prentice Hall

19. Vallet B, Lévy B (2008) Spectral Geometry Processing with Manifold Harmonics. Comput Graph Forum 27:251–260. https://doi.org/10.1111/j.1467-8659.2008.01122.x

20. Jost J (2011) Riemannian Geometry and Geometric Analysis, 6th ed. Springer-Verlag, Berlin Heidelberg

21. Crane K, de Goes F, Desbrun M, Schröder P (2013) Digital Geometry Processing with Discrete Exterior Calculus. In: ACM SIGGRAPH 2013 Courses. ACM, New York, NY, USA, pp 7:1–7:126

22. Duque-Antón M (1997) Constructing efficient simulated annealing algorithms. Discrete Appl Math 77:139–159. https://doi.org/10.1016/S0166-218X(96)00132-1

23. Har-peled S (2011) Geometric Approximation Algorithms. American Mathematical Society, Boston, MA, USA